



HAL
open science

Functional impact of oxygen-saturated zeolite nanoparticles on macrophages in the context of glioblastoma: an in vitro and in vivo study

Aurélie E Ferre, Sarah Komaty, C H elaine, Cl ement Anfray, Sajjad Ghojavand, Julie Coupey, Romaric Saulnier, Benoit Bernay, Laurent Chazalviel, Svetlana Mintova, et al.

► To cite this version:

Aur elie E Ferre, Sarah Komaty, C H elaine, Cl ement Anfray, Sajjad Ghojavand, et al.. Functional impact of oxygen-saturated zeolite nanoparticles on macrophages in the context of glioblastoma: an in vitro and in vivo study. *Colloids and Surfaces B: Biointerfaces*, 2023, 230, pp.113524. 10.1016/j.colsurfb.2023.113524 . hal-04190367

HAL Id: hal-04190367

<https://normandie-univ.hal.science/hal-04190367>

Submitted on 29 Aug 2023

HAL is a multi-disciplinary open access archive for the deposit and dissemination of scientific research documents, whether they are published or not. The documents may come from teaching and research institutions in France or abroad, or from public or private research centers.

L'archive ouverte pluridisciplinaire **HAL**, est destin ee au d ep ot et  a la diffusion de documents scientifiques de niveau recherche, publi es ou non,  emanant des  tablissements d'enseignement et de recherche fran ais ou  trangers, des laboratoires publics ou priv es.

Colloids and Surface B: Biointerfaces

Functional impact of oxygen-saturated zeolite nanoparticles on macrophages in the context of glioblastoma: an *in vitro* and *in vivo* study.

Ferre E. Aurélie¹, Komaty Sarah², Hélaine Charly¹, Anfray Clément¹, Ghojavand Sajjad², Coupey Julie¹, Saulnier Romaric³, Bernay Benoit⁴, Chazalviel Laurent¹, Mintova Svetlana^{2*}, Valable Samuel^{1*}

¹Normandie Univ., UNICAEN, CNRS, ISTCT, GIP CYCERON, 14000 Caen, France.

²Normandie Univ., UNICAEN, CNRS, ENSICAEN, Laboratoire Catalyse et Spectrochimie, 14000 Caen, France.

³UAR3408/US50 (Unicaen-CNRS-INSERM-CEA) Cyceron, GIP Cyceron, 14000 Caen, France.

⁴ Normandie Univ., UNICAEN, Proteogen, US EMerode, 14000 Caen, France.

* *Correspondence:*

*Samuel Valable (samuel.valable@cnrs.fr)

ISTCT, GIP CYCERON, Bd H Becquerel, BP 52259; 14074 Caen, France

*Svetlana Mintova (mintova@ensicaen.fr)

LCS, ENSICAEN; 6, boulevard Maréchal Juin ; 14050 Caen, France

Statistical summary:

Words: 8,262

Figures: 8

ABSTRACT

In the context of glioblastoma (GBM), hypoxia and inflammation are two main players of the tumor microenvironment. Hypoxia stimulates various features involved in tumor growth and also maintains a specific environment that favors protumor macrophages. Therefore, targeting hypoxia could potentially restore an anti-tumor M1 phenotype in macrophages. Besides, iron demonstrated its capacity to stimulate the polarization of macrophages towards an M1-like phenotype. In this paper we took advantages of microporous nanoparticles to co-deliver both oxygen and iron to bone marrow derived macrophages (BMDM) enabling the investigation of changes in polarization status and proteomic profiles. The nanoparticles were used in two *in vivo* models of glioblastoma, specifically, in both immunodeficient and immunocompetent settings. Our *in vitro* findings revealed that iron doped nanoparticles, saturated with oxygen were deemed safe for macrophages but did not demonstrate the capacity to change the M1 or M2 phenotypes. However, these nanoparticles induced some changes in proteomics pathways. The present study reports on *in vivo* experimentation that revealed the effects of nanoparticles on the hypoxic fraction, tumor volume, and macrophage phenotype in a GBM model. The findings indicated that the presence of nanoparticles led to a reduction in the hypoxic fraction in one of the GBM models, while no significant changes were observed in the tumor volume or macrophage phenotype. The present data showed that nanoparticles possess the capability of delivering both oxygen and iron to macrophages; though, they do not possess the ability to effectively repolarize M2 macrophages. Such strategies could be used in conjunction with other potent molecules to avoid M1 macrophages to inevitably differentiate to M2 macrophages.

Keywords

Nanosized zeolite, Macrophages, hypoxia, Glioblastoma.

1. Introduction

Glioblastoma (GBM) is one of the most aggressive tumors in adults with a median survival of around 15 months [1]. Along with the tumor cells, it is known that the tumor microenvironment (TME) stimulates tumor growth and limits the treatments efficacy causing many recurrences [2]. Among this microenvironment, hypoxia and tumor-associated macrophages (TAMs) are two main interrelated components.

Hypoxia, which denotes a reduced availability of oxygen pressure in a given environment or tissue, appears during tumor development in many solid tumors and is much more pronounced in high grade glioma than in lower grade gliomas [3]. In the context of GBM, the oxygen tissue pressure (p_{tO_2}) is known to be less than 5 mmHg while being around 40 mmHg in the healthy brain tissue [4–6]. More importantly, hypoxia is not a binary phenomenon and oxygen gradients should rather be considered [7]. Hypoxia can be attributed to an increase in metabolic demand of tumor cells as well as restructured and inadequately functional vasculature resulting from the process of tumor angiogenesis [8]. This lack of oxygen in the GBM contributes to tumor progression and its resistance to radio-chemotherapeutic interventions [9–11]. Recently, various strategies have been developed to alleviate tumor hypoxia, if only transiently, either using passive reoxygenation [12–14] or targeted strategies based on the use of nanoparticles (NPs)[15] as carriers of gases to deliver oxygen to the tumor bulk in a selective manner.

The GBM microenvironment is also composed of immune cells [16]. Among immune cells, TAMs are the most abundant cells and mainly originate from monocyte-derived macrophages (MDM) recruited from the peripheral circulation [17]. Macrophages ($M\theta$) are highly plastic cells and adapt their phenotypes to their environment. TAMs mainly display a pro-tumoral M2-like phenotype (M2 $M\theta$), which is immunosuppressive, and a minority display an anti-tumoral M1-like phenotype (M1 $M\theta$)[18].

Many studies showed that the presence of M2 $M\theta$ is correlated with poor prognosis in various cancer and that M2 $M\theta$ depletion or re-education to a M1 $M\theta$ phenotype would be beneficial against tumor progression [19–21]. Among the various drivers toward an M2 phenotype, it is known that

hypoxia influences macrophage fate towards a M2-like phenotype [21]. Consequently, targeting both TAMs polarization and tumor oxygenation could provide a novel approach to develop therapeutic strategies against cancer [19,22].

In our previous studies, we demonstrated that the highest oxygen release from microporous aluminosilicate nanoparticles (Faujasite, zeolite X) occurs when the oxygen pressure in the environment of the NP decreases [15]; which is of great interest for GBM where the tissue pO_2 is very low. This becomes a very attractive strategy to provide oxygen to hypoxic tissues which could be used to re-educate M2 M θ cells which are mostly located in the most hypoxic region of the GBM as we previously demonstrated [21].

Interestingly, some studies showed that NPs could also act more directly on macrophages. As an example, iron-based NPs (SPION) can prime the polarization of M θ from M2 M θ to M1 M θ [23] and this strategy was also demonstrated *in vivo* in a model of Lewis lung carcinoma [24].

Herein, we used oxygen-saturated Fe-containing zeolite X nanoparticles (Oxy Fe-X) to increase the oxygen availability in the TME and to provide iron to TAMs, considered as a dual strategy designed to polarize M2 M θ to an M1 M θ phenotype. The excellent biocompatibility, non-toxic nature and remarkable stability of zeolite nanoparticles render them a highly promising option for biomedical applications[15]. First, we analyzed the effect of oxygen free as synthesized zeolite nanoparticles (sample Fe-X) and the oxygen-saturated zeolite X containing iron (sample Oxy Fe-X) on M θ toxicity and phenotype of macrophages *in vitro*. Then, we followed *in vivo* their functional impact on the TME and the TAMs in GBM-bearing mice. We used a preclinical human GBM model developed on immunodeficient mice and a preclinical murine GBM model inoculated in immunocompetent syngenic mice.

2. Experimental section

2.1 Preparation of nanosized faujasite (Na-X) type zeolites

Stable suspension of nanosized zeolite (Na-X) was prepared from colloidal precursor solution under hydrothermal conditions as described previously [15,25]. The as-prepared precursor suspension of Na-X zeolite was kept at room temperature for 24 h, followed by dehydration using freeze-drying method prior to hydrothermal treatment at 50°C for 26 h. After the hydrothermal treatment, the zeolite nanoparticles were purified and redispersed in double distilled water; the pH of the suspension containing nanosized zeolite crystals was almost 7 and the concentration was 25 mg/mL.

2.2 Preparation of iron containing nanosized faujasite (Fe-X) type zeolites

The purified Na-X zeolite suspension (pH \approx 7) was ion exchanged using iron nitrate ($\text{Fe}(\text{NO}_3)_3 \cdot 9\text{H}_2\text{O}$) following the procedure: 25 mL of $\text{Fe}(\text{NO}_3)_3 \cdot 9\text{H}_2\text{O}$ (3 mM) was added in 5 mL of Na-X suspension (25 mg/mL solid concentration). The suspension was then kept under stirring at room temperature for 1 h and then washed by double distilled water [25]. This procedure was repeated three times to finally obtain the Fe-X zeolite suspension with pH=7.

2.3 Characterizations of nanosized zeolites

Powder samples (Na-X, Fe-X) were measured using a PANalytical X'Pert Pro diffractometer with $\text{CuK}\alpha$ monochromatized radiation ($\lambda = 1.5418 \text{ \AA}$). The samples were scanned in the range of 4-50 $^{\circ}2\theta$ with a step size of 0.02 $^{\circ}$. The crystal size, morphology and crystallinity of samples were determined by a transmission electron microscopy (TEM) using a JEOL 2010 FEG and a FEI LaB6 TECNAI G2 30UT operated at 200 kV and 300 kV, respectively. In addition, the chemical composition of the samples was determined by Inductively Coupled Plasma mass spectrometry (ICP-MS) using a 7900 ICP-MS from Agilent Technologies. The hydrodynamic diameter and zeta potential values of the zeolite nanoparticles in water suspension were determined using Malvern Zetasizer Nano Dynamic Light Scattering (DLS). The analyses were performed on samples after purification with a solid concentration of 10 mg/mL. Nitrogen adsorption/desorption isotherms of the zeolite powders were measured using Micrometrics ASAP 2020 volumetric adsorption analyzer. Samples were degassed at 250 $^{\circ}\text{C}$ under

vacuum overnight prior to the measurement. The external surface area and micropore volume were estimated by alpha-plot method. The micropore and mesopore size distributions of solids were extracted from adsorption branch by the Nonlocal Density Functional Theory (NLDFT) and from the desorption branch using the Barret-Joyner-Halenda (BJH) algorithm, respectively.

2.4 Loading of oxygen in nanosized Fe-X zeolite

The Fe-X zeolite suspension was loaded with O₂ under bubbling with a flow rate of 0.8 mL/min for 30 min. The oxygenated zeolite suspension was named "Oxy-Fe-X".

2.5 Release of oxygen from nanosized zeolite crystals in aqueous and hypoxic conditions

The oxygen release capacity of nanosized Fe-X and Oxy-Fe-X zeolites was studied in a hypoxia workstation (IN VIVO 2 500, Baker Ruskinn, Alliance Bio Expertise, Guipry, France) set at 0.1% oxygen at 37°C. PBS (Phosphate buffered saline, Sigma-Aldrich, St Quentin-Fallavier, France) solution was equilibrated with the gas mixture contained in the hypoxia chamber for 1 h prior to the experiment. A closed reaction vessel containing 12 mL of equilibrated PBS at 37°C, and a dissolved oxygen sensor (SevenGo (Duo) pro™ / OptiOx™, Mettler Toledo, Columbus, USA) was placed inside the hypoxia chamber. Prior to the experiments, baseline was established by measuring the oxygen saturation in the system for 30 min. 500 µL of nanosized zeolites (4%) were then added to the system, and the oxygen dissolved in the PBS solution was measured continuously for 1 h.

2.6 Bone marrow-derived macrophage culture and activation

Bone marrow was isolated from the tibiae and femurs of Swiss mice (≈ 30g, CURB, Cyceron). Bone marrow was flushed with Iscove's Modified Dulbecco's Medium (IMDM, Gibco) solution supplemented with 60 % FetalClone II (FCII, Hyclone, Fisher Scientific) and 100 U/mL penicillin and 100 µg/mL streptomycin. The marrow was passed through a 70 µm strainer and M θ (M0) were selected and cultured in IMDM enriched with 15% FCII, 100 U/mL penicillin and 100 µg/mL streptomycin, 10 ng/mL recombinant mouse M θ colony-stimulating factor (M-CSF, PeproTech France, Neuilly-sur-seine, France) and 10 ng/mL recombinant mouse Fms-related tyrosine kinase three ligand (Flt3-Ligand, PeproTech) at 37°C in a humid atmosphere. M1 M θ cell were obtained by culturing in 1 g/L glucose

DMEM (Sigma-Aldrich) supplied with 15% FCII, 100 U/mL penicillin and 100 µg/mL streptomycin, 2 mM Gln (Sigma-Aldrich), 100 ng/mL LPS (Sigma-Aldrich) and 10 U/mL recombinant mouse IFN γ (PeproTech). M2 M θ cells were obtained by culturing with 1 g/L glucose DMEM supplemented with 15% FCII, 1% P/S, 2mM glutamine (Sigma-Aldrich) and 50 ng/mL recombinant mouse IL-4 (PeproTech).

2.7 Cell culture

The murine glioblastoma cell line GL261 (NCI-DCTD (Division of Cancer Treatment and Diagnosis), Repository) and human glioblastoma U251-MG (Cellosaurus CVCL_0021) purchased from National Cancer Institute (NCI, Bethesda, MD, USA) were used in this study. GL261 cells were maintained in RPMI medium (Roswell Park Memorial Institute, Sigma-Aldrich) supplemented with 10% fetal calf serum (Eurobio, Courtaboeuf, France), 2 mM L-glutamine, and 100 U/mL penicillin and 100 µg/mL streptomycin at 37°C with 5% CO $_2$ and 95% air. U251-MG were cultured in DMEM 1 g/L of glucose supplemented with 10% fetal calf serum, 2 mM L-glutamine, 100 U/mL penicillin and 100 µg/mL streptomycin at 37°C in 5% CO $_2$ and 95% air.

Cells exposure to nanosized zeolite crystals

The cells were exposed to zeolites in the form of colloidal suspensions using water solvent added directly to their culture medium. The control condition corresponds to the addition of the same volume of water to the culture medium free of zeolites.

Analysis of cell cycle

All flow cytometry experiments were performed on a Gallios TM flow cytometer (Beckman Coulter SAS, Villepinte, France) and analyzed with Kaluza[®] software (Beckman Coulter SAS) from the US PLATON platform of the Normandy University - Caen.

Cell preparation for cycle analysis required recovering cells from the cell line as well as cells floating in the supernatant. The cells were detached using a scraper as described previously. The cells were then rinsed with PBS, fixed with 70% ethanol and stored at 4°C. After rinsing with PBS, the cells were labeled with propidium iodide (PI) using the DNA-prep reagents kit (Beckman Coulter) according to the supplier's instructions.

Analysis of cell viability

After treatment, the cells were rinsed with cold PBS and fixed with a solution of crystal violet (2.3%) and ethanol (20%) (Sigma-Aldrich) for 30 min. Then, the cells were rinsed three times with tap water. After complete drying, the cell membranes were broken with an acetic acid solution (10%) in order to release crystal violet from the cells. The optical density of the solution was then analyzed by spectrophotometry on SPARK® reader (Tecan, Männedorf, Switzerland) at a wavelength of 600 nm.

Determination of nitric oxide (NO) production

Measurement of NO in the SN of M θ cultures was performed by the Griess reaction. Briefly, the Griess reagent was prepared by mixing 2% sulphanilamide (Sigma-Aldrich) in 10% phosphoric acid (Sigma-Aldrich) and 0.2% naphthylethylene-diamine-dihydrochloride (Sigma-Aldrich). The reagent was added to SN and the mixture was incubated 10 min at room temperature in the dark. Each sample was assayed in duplicate, the absorbance was measured at 540 nm and NO concentration was determined with sodium nitrite as a standard.

Determination of Arginase 1 (Arg1) activity

Arg1 activity was determined by a standard colorimetric method in cell lysates. Briefly, cells were lysed by adding 0.1% Triton X-100 (Sigma-Aldrich) and 50 mM Tris-HCl (pH 7.5). 10 mM MnCl₂ (Sigma-Aldrich) to cell samples, then heated at 56°C for 7 min to activate the enzyme. Hydrolysis of L-arginine by Arg1 was performed by incubating the mixture with 50 μ mol of L-arginine (pH 9.7; Sigma-Aldrich) at 37°C for 2 h, and the reaction was stopped by adding an acid solution (H₂SO₄; H₃PO₄; H₂O). For the determination of urea production, α -isonitrosopropiophenone (Sigma-Aldrich) was added and the mixture was incubated at 95°C for 30 min and then 4°C for 30 min. Each sample was assayed in duplicate, the absorbance was measured at 540 nm and urea production was determined with urea as a standard.

2.8 Analysis of protein expression

Protein extraction was performed with an extraction buffer containing 50 mM TrisHCl, 150 mM NaCl, 1% Triton X100, 0.1% Sodium Dodecyl Sulfate. The lysate was centrifuged at 10000g for 30 minutes at

4°C. The proteins were quantified. For proteomic analysis, 5 µg of each sample was prepared according to a modified GASP protocol [26] before being digested, at 37°C overnight, with an enzymatic cocktail of Lysine C and trypsin. The peptides were then concentrated in a C18 micro-column before injection. First, the peptides were fractionated on a UHPLC NanoElute (Bruker Daltonics) according to a gradient of 80 minutes (from 2 to 30% of B in 70 min, increase to 37% of B in 5 min then to 85% in 5 min at a flow rate of 250 nL/minute followed by a washing step at 300 nL before re-equilibration (buffer A: H₂O, 0.1% formic acid (FA); buffer B: Acetonitrile, 0.1% FA)). The mass spectrometry analyzes were carried out on a TIMSTOF-Pro type instrument (Bruker) in PASEF mode, in the range of m/z 100-1700 and 1/K0 0.75-1.25, with exclusion of monocharged ions. The data thus obtained were first analyzed by the Preview software (ProteinMetrics) in order to estimate the quality of the enzymatic digestion carried out and to predict the post-translational modifications present. The library search was then carried out by the PeaksX+ software on the basis of the fragmentations obtained in MSMS using the updated proteome (Uniprot) of *Mus musculus*. The trypsin parameter was selected and the mass error is fixed at 20 ppm in MS and 0.05 Da in MSMS. The relative quantification by Label Free method (LFQ) was carried out using the XIC (extracted ion chromatogram) with retention time alignment. The data was then transferred to the Perseus software (<https://maxquant.net/perseus/>) in order to filter the data according to different parameters (>1 peptide), implement the missing values and perform the statistical analysis via a t-test of Student or an ANOVA. Lastly, the results were transferred to Genoppi (<https://www.lagelab.org/genoppi/#>) in order to draw the Volcano Plot. The differentially expressed proteins were thus filtered according to the parameters p value<0.001 and ratio>1.5. The heatmap was produced, with a Spearman method, using the ComplexHeatmap package from the R software. The accessions corresponding to the proteins thus obtained were used to carry out the various enrichments, using a Bonferroni method, in GO (MF, BP) and Kegg via ClueGo app from Cytoscape software. The “ko number” of identified proteins was used to search for signaling pathways using the web application Kegg mapper (<https://www.genome.jp/kegg/mapper.html>). iNOS was detected with the accession number #P29477 and Arg1 with #Q1176.

2.9 Animal studies

Animal investigations were performed under the current European directive (2010/63/EU). Ethical approval was obtained by S.V from the regional committee (CENOMEXA) and the French Ministère de l'Enseignement Supérieur, de la Recherche et de l'Innovation with the authorization APAFIS#12727.

GBM preclinical model

Six-week-old nude male mice (30-40 g, Charles River Laboratories) were used for U251-MG cells and C57BL/6 male mice (20-30 g, Janvier Laboratory) for GL261 Cells. Mice were housed at the Specific-pathogen-free ONCOModels platform (Cyceron, Caen, France).

Mice were anesthetized with 5% isoflurane for induction and 2% during surgery in a mixture of 70% nitrous oxide and 30% O₂. The depth of anesthesia was assessed beforehand by the foot reflex. The mice were then placed in a stereotactic frame after an application of xylocaine gel on the ear bars. A burr hole of 1 mm diameter was drilled in the skull at 2 mm lateral 0 mm anteroposterior and 4 mm depth according to the Bregma. U251-MG ($5 \cdot 10^4$ cells) or GL-261 ($1 \cdot 10^5$ cells) were injected using a dental needle (30 G; 0.3×23 mm) at a flow rate of 0.6 μL/min for 5 min. The needle was withdrawn after 5 min to avoid cell reflux. At the end of the procedure, the animal was sutured and painkilled (BupreCare® 0.05 mg/kg, subcutaneously).

MRI studies

The mice were anesthetized during the MRI acquisition as described previously. The animal was placed in a ventral position in a cradle heated to 37°C, the animal's breathing was also monitored using a sensor placed under the abdomen of the mouse. The images were acquired on the CYCERON imaging platform with a high magnetic field 7 Tesla PharmaScan® MRI (Bruker, Ettlingen, Germany) system specially designed for small animals. Data acquisition was performed using Paravision software (version 6.0.1) (Bruker). Anatomical imaging was then obtained with a T2w Rapid Acquisition with Relaxation Enhancement (RARE) sequence, the parameters of which were: acceleration factor of 8; TR/TE effective = 5000/60 msec; number of experiments (NEX) = 1; 20 sections of 0.5 mm thickness;

spatial resolution = 0.07 x 0.07 mm and a total acquisition time: 2 min. The tumor volume was then delineated manually using the ImageJ software [27].

Injection of zeolite suspensions

The zeolites in saline suspensions were prepared with a concentration of 5 mg/mL. The zeolite suspensions were injected using two different procedures, depending on the mouse strain concerned. The injections were carried out intravenously percutaneously in the tail vein for the nude mice or in the retro-orbital vein for the C57BL/6 mice.

Immunohistochemistry

After analgesia with buprenorphine, the animals were deeply anesthetized at a sub-lethal dose, followed by a thoracotomy and an intracardiac infusion of cold and heparinized saline. The brain was then extracted from the cranial box then immersed briefly (5 sec) in cold n-pentane (Sigma-Aldrich) before freezing at -80°C. The brains were cut in a cryostat in order to make coronal sections 30 µm thick. The sections were mounted on superfrost slides (Thermo Fisher Scientific), in a serial manner, then stored at -80°C before the immunohistological analyses.

After thawing, the slides supporting the histological sections were post-fixed for 30 min in a 4% paraformaldehyde solution (Sigma-Aldrich). The slides were then rinsed with PBS and then incubated for 2 h at room temperature with a blocking solution composed of PBS, 0.5% 100X triton (Sigma-Aldrich), 0.1% tween (Sigma-Aldrich), 3% bovine serum albumin (BSA; Sigma-Aldrich). The sections were then incubated at 4°C overnight in a solution of PBS, 0.5% triton X100, 0.1% tween-1%, 1% BSA, containing the primary antibodies rat anti-CD68 (1:1000, Abcam, ab53444), rabbit anti-CD206 (1:1000, Abcam, ab252921); rabbit anti-CAIX (1:100, Abcam, ab10471). After rinsing with PBS-tween-triton, the sections were incubated at room temperature for 1 h, in the presence of the secondary antibody conjugated to a fluorochrome and Hoechst 33342 (10 µg/mL, Sigma-Aldrich) in a solution of PBS, 0.5% triton X-100, 0.1% tween, 1% BSA, and then mounted on the slides with Aqua-Poly/Mount mounting medium (Tebu-bio, Le Perray-en-Yvelines, France). The mosaics were produced on a DMI8S

fluorescence microscope (Leica microsystems, Wetzlar, Germany) with MetaMorph® software and analyzed with ImageJ software [27].

Images analysis and quantification

All analyses were performed with regions of interest corresponding to peritumoral region of the tumor. After application of automatic threshold, images were binarized with ImageJ software. The results obtained were represented as the percentage of immunostaining in the ROI.

2.10 Statistical analyses

All data were expressed as mean \pm standard deviation (SD). All statistics were performed with Statistica Software® (Tibco Software Inc; USA). Tests used and the number of experiments were detailed in each figure legend.

3. Results and Discussion

The chemical composition, powder X-ray diffraction (XRD), size and zeta potential of the zeolite nanocrystals used in this work are provided in **Table S1 and Figure S1**. As quantified by DLS, the nanosized zeolite crystals in water suspension (a concentration of 10 mg/mL) have an average size of 20 nm. The zeta potential of the zeolite nanocrystals in water suspension is ≈ 40 mV, which corresponds to highly stable negatively surface charged particles. ICP-MS confirmed the presence of 1% of Fe in the Fe-X zeolite sample as we already described [25]. Incorporation of Fe into the zeolite did not induce any remarkable change in the crystal's properties including size, shape, porosity and surface charge. XRD of the two zeolite samples show patterns with broadened peaks reflecting the small particle size as confirmed by the TEM images. Typical Bragg peaks corresponding to FAU-type zeolite present in the Na-X sample (**Figure S1A**) is perfectly preserved after ion exchange treatment. The porosity of zeolite nanoparticles before and after ion exchange treatment was investigated by N₂ sorption analysis (**Figure S1B**). All the two samples exhibit similar features: Type I isotherm at low P/P₀ characteristic for microporous materials and high adsorption uptake at P/P₀ > 0.8 reflecting the high textural mesoporosity of closely packed zeolite nanoparticles with similar particle sizes. The nanosized zeolites have an average size of 15-20 nm measured in water suspension (**Figure S1C**) and surface charge (ζ) of -43 to -45 mV (**Figure S1D**).

3.1 Impact of zeolites on macrophages viability: in vitro study

We first aimed to analyze the effect of zeolite nanocrystals on bone marrow-derived macrophages (BMDM) viability. M0, M1 and M2-polarized M θ were exposed to Na-X or Fe-X zeolites with different concentrations (10 or 100 μ g/mL); the cell morphology, density and cell cycle were assessed at 24 h. As already described [28,29], in normoxia and in hypoxia (0.2% oxygen), we observed less cell number in M1 M θ than M0 and M2. Regardless of the concentration employed, **Figure 1** depicts that the presence of Na-X zeolite nanocrystals did not generate any detectable modifications in the morphology or density of cells in M0, M1, and M2 M θ .

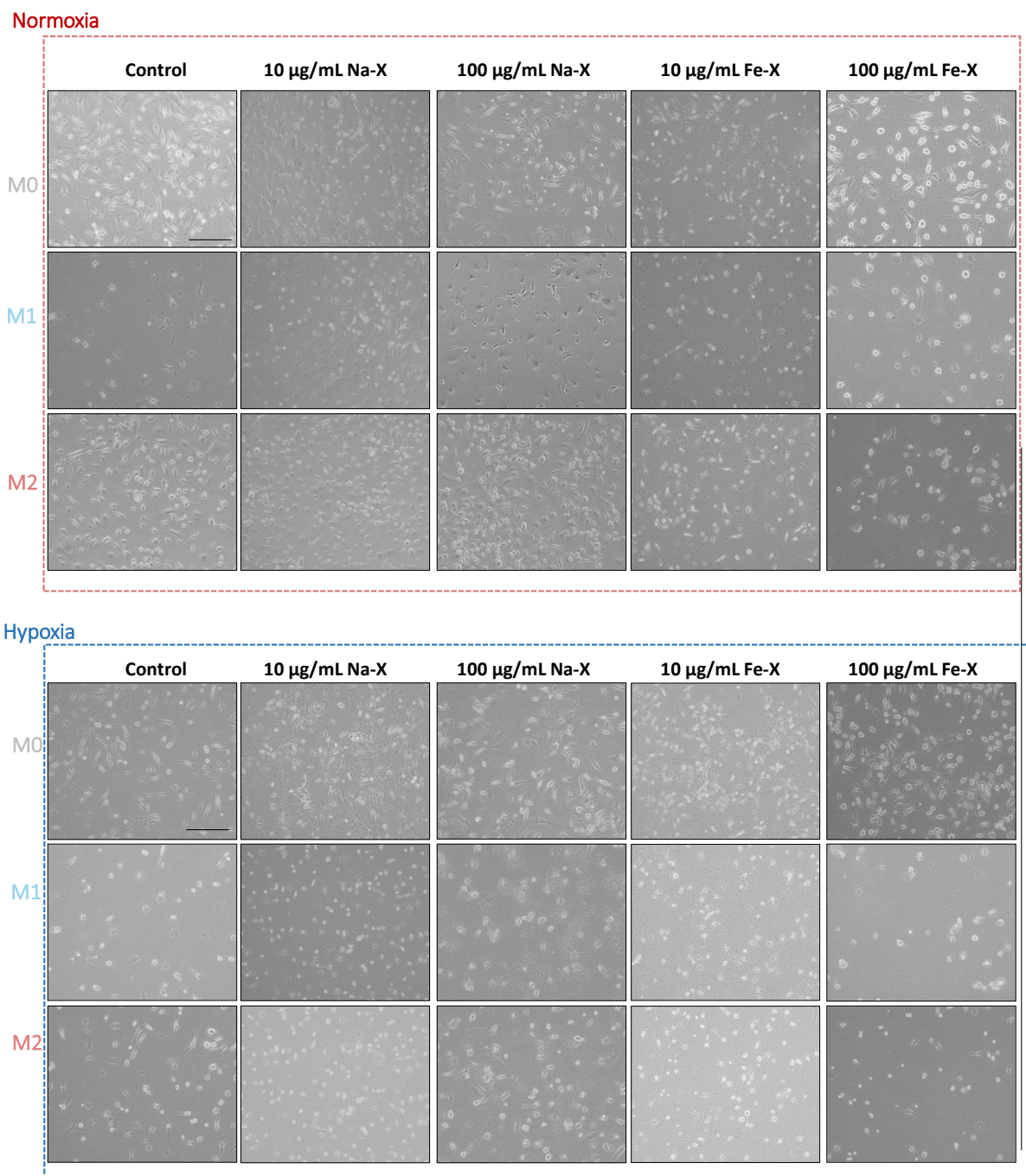


Figure 1: Impact of zeolites on bone marrow derived-macrophages morphology. Representative images of bone marrow derived-macrophages (BMDM) after 24 hours exposure to increasing concentration of as prepared zeolites (Na-X) or Fe-exchange zeolite (Fe-X) in normoxia (21% O₂) and hypoxia (0.2% O₂). Scale bar =100 µm.

Figure 2A and B demonstrate that the hypoxic environment with 100 µg/mL of Na-X zeolite resulted in a greater accumulation of cells arrested in the subG1 phase of their cell cycle, suggesting the presence of apoptotic cells. However it should be noted that this effect did not reflect any noticeable alterations in cell density or morphology.

Fe-X zeolites showed more pronounced effect on macrophages. Our observations revealed that the utilization of 100 µg/mL Fe-X resulted in a noticeable transformation in cell morphology and density. Specifically, an increase in cell size and roundness was noted, concomitant with a significant reduction in cell density. ($85.1 \pm 1.6\%$ for M0 and $65.0 \pm 13.9\%$ for M2 in normoxia; $53.9 \pm 5.3\%$ for M2 in hypoxia relative to their respective control phenotype) (**Figure 1**). The changes in the cell density for M0 and M2 were observed in the cell cycle. In M0 and M2 M θ cells, subjected to normoxia and hypoxia conditions, a dose-dependent cell cycle arrest in the subG1 phase was observed at concentrations of 10 and 100 µg/mL (**Figure 2**).

No significant alterations in morphology and density were noted for M1 M θ . Interestingly, M1 M θ cell cycle was affected by the presence of 10 µg/mL of Fe-X zeolites, while no such effect was detected at 100 µg/ml Fe-X (**Figure 2**). Altogether, these experiments show that, in normoxic condition, Na-X zeolites are safe for all M θ phenotypes. Fe-X zeolites may have more impact on the cell cycle for all phenotypes and this effect seems dose-dependent for M0 and M2. These changes in cell cycle were paralleled by a decrease in the cell number for these two phenotypes.

Under hypoxic condition, the cells exhibited greater sensitivity to the presence of both types of zeolites. However, we observed that the Fe-X nanoparticles were more deleterious at the lower concentration, especially on M1 M θ (**Figure 2**). The majority of investigations employing iron based-NP aimed to re-educate M2 M θ [30]. Herein, we show that these iron based-NP at high concentration could also be used to kill M2 M θ . This effect is not full in line with the findings reported in reference [31]. In this paper, BMDM were exposed to amorphous silica or SPION in the same range of the concentration that we used and no toxicity was observed. In our study, it was observed that the

cytotoxic effect of iron doped nanozeolites on M2 M0 was more pronounced under hypoxic condition. One could argue that the latter phenotype exhibited a higher uptake of zeolites, but findings reported in **Figure S2** using fluorescent nanozeolites [32], indicate comparable cytoplasmic uptake among all three phenotypes.

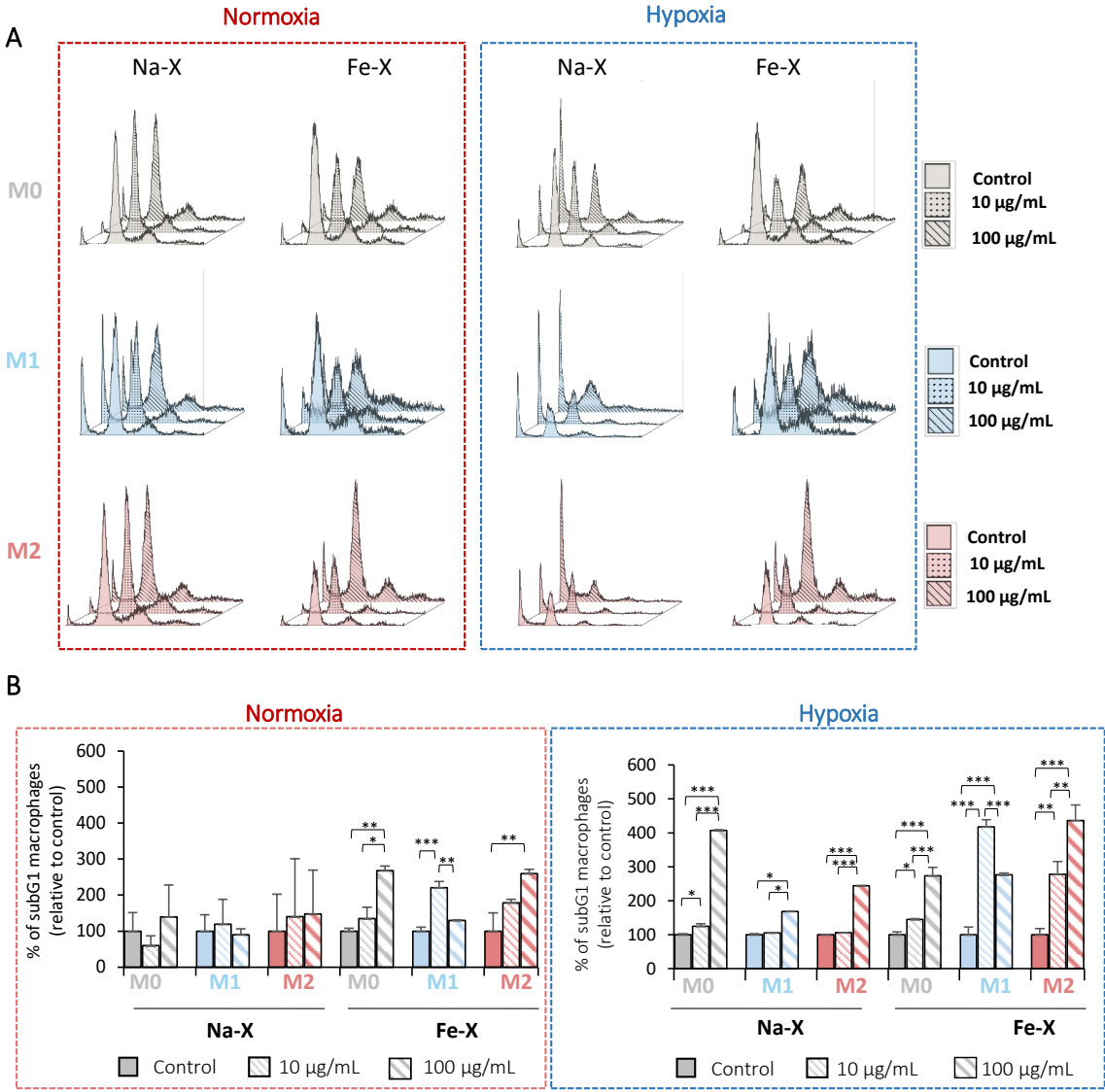


Figure 2: Impact of zeolites on the cell cycle. A) Cell cycle profiles of M0, M1 and M2 macrophages, exposed or not to Na-X or Fe-X zeolites at increasing concentrations in normoxia (21% O₂) or hypoxia (0.2% O₂). B) Quantification of Sub-G1 phase in macrophages exposed to increasing concentration of as prepared (Na-X) and Iron doped (Fe-X) nanozeolites. Mean ± standard deviation, N=3. * p < 0.05; ** p < 0.005; *** p < 0.001. Tukey's HSD test after significant one-way ANOVA (treatment).

3.2 Impact of zeolites on macrophages polarization

The next focus was on the M θ polarization status in the presence of nanosized Na-X, Fe-X and Oxy-Fe-X zeolites (oxygen saturated Fe-X nanozeolites). The oxygen releasing properties of Oxy-Fe-X when placed in saline solution previously stored in hypoxic environment (0.1% of oxygen) is presented in **Figure 3**. We confirmed the great oxygen release capacity of Oxy-Fe-X zeolite relative to the oxygen deficient Fe-X sample.

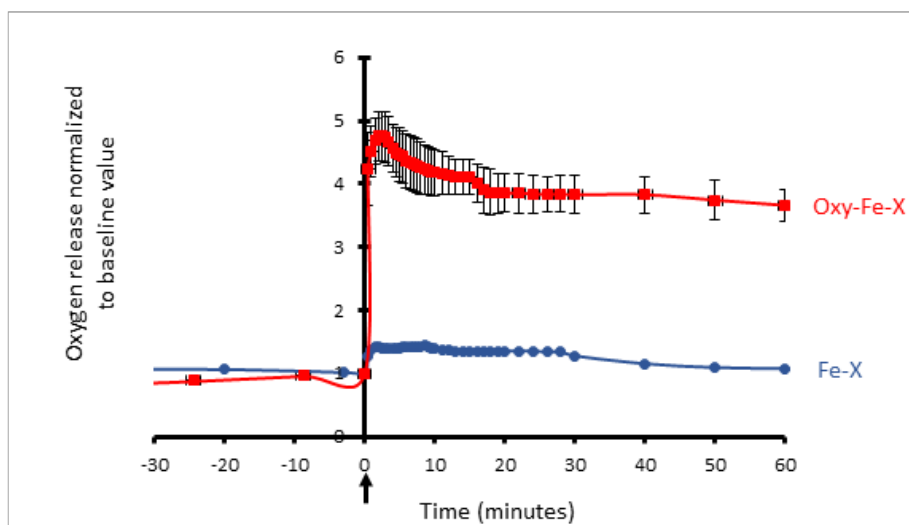


Figure 3: oxygen release experiments. Quantification of oxygen released from zeolites in aqueous solution (phosphate buffered saline) kept in a hypoxic workstation at 0.2% of oxygen. N=3 Oxy-Fe-X; N=1 Fe-X.

Subsequently, we evaluated the activation status of M θ following incubation in the presence of zeolites with and without oxygen loading. As expected and based on reported results [28], under normoxic condition, M1 M θ produced high amount of the M1 phenotype marker Nitric oxide (NO) ($1.4 \pm 0.4 \mu\text{M}$ of NO in the culture medium) while M0 M θ and M2 M θ did not display a comparable response (**Figure 4 A**). When nanosized Na-X, Fe-X or Oxy-Fe-X zeolites were introduced, the NO production by M1 M θ remained stable at approximately $1.3 \mu\text{M}$. However, the presence of zeolites did not show any significant effect on the NO production by both M0 and M2. In hypoxic conditions, the NO synthesis

by M1 M θ was around 0.4 μ M and remained unaffected by the presence of the three types of zeolites. A decrease of NO production in hypoxic condition has already been reported by us and others [28]: M0 and M2 demonstrating no detectable level of NO. Based on the NO production assay, the supply of O₂ by Oxy-Fe-X did not influence on the phenotype of M θ that remained unaltered under both normoxic and hypoxic conditions.

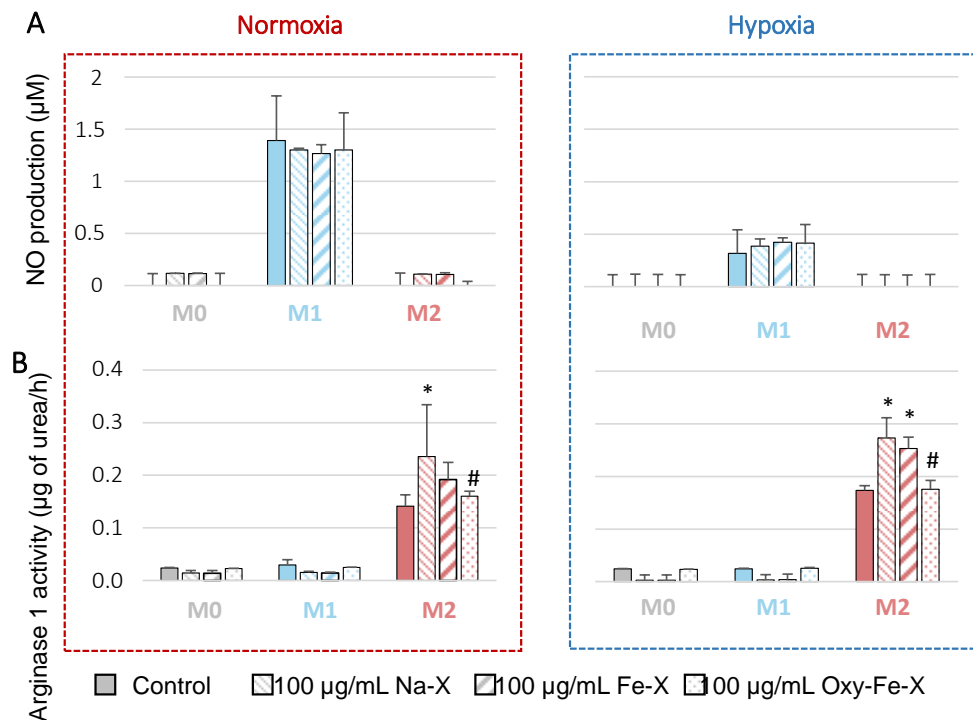


Figure 4: Impact of zeolites on macrophage polarization. A) Quantification of nitric oxide (NO) production. Mean \pm standard deviation, N=3. One-way ANOVA (treatment) not significant. **B)** Quantification of urea production per hour by Arginase 1. Mean \pm standard deviation, N=3. One-way ANOVA (treatment) not significant. * p < 0,05 vs control, # p < 0,05 vs NaX

In order to assess the polarization state of M2 M θ , we quantified urea production, which reflects the Arginase 1 activity (13), active exclusively in the M2 phenotype. The results show that the production of urea by M2 M θ was 0.14 ± 0.022 μ g/h while M0 and M1 produce 0.023 ± 0.001 and 0.029 ± 0.01 μ g/h of urea, respectively in normoxic condition (**Figure 4 B**). After addition of 100 μ g/mL Na-X to the medium in normoxic condition, the urea production by M2 M θ increased slightly to reach 0.24 ± 0.09

µg/h after 24 h. The change was observed for Fe-X and Oxy-FeX zeolites. In line with our previous report [28], under hypoxic condition, the urea production by M2 Mθ was increased and reached 0.17 ± 0.01 . In the presence of Na-X and Fe-X, the urea produced by M2 Mθ was higher, *i.e.* 0.27 ± 0.03 and 0.25 ± 0.02 , respectively. Interestingly, both in normoxic and hypoxic conditions, the presence Oxy-Fe-X reversed the urea synthesis induced by the Na-X sample.

In summary, our analysis on the two metabolic pathways studied showed that the presence of sodium or iron-based nanosized zeolites did not elicit any significant modifications in the characteristics of each phenotype. Interestingly, we show that the presence of oxygen-saturated Oxy-Fe-X, lead to the reduction in the level of Arginase activity compared M2 Mθ treated with Na-X zeolites. Nonetheless, we were unable to reverse the production of urea by untreated M2 Mθ. In the literature, the most discussed effect of M2 reeducation is based on the use of iron oxide nanoparticles [33]. However, based on previous reported study [24], the authors noted that the reprogramming of M2 Mθ could be rather mediated by the presence of iron itself.

One of the major limitations of the above-mentioned studies is that it is mostly performed in normoxic conditions. As already discussed, hypoxia is a driving force that enhancing the M2 phenotype and prompting the transition of M1 to an M2 phenotype [28]. In order to elucidate a potential effect of Fe-X and Oxy-Fe-X zeolites on Mθ, we performed a proteomic study in hypoxia for both M1 and M2 Mθ.

3.3 Impact of zeolites on macrophages proteome in hypoxic conditions

Fe-X zeolite crystals induced a change in the expression of numerous proteins in comparison to the untreated control groups of M1 Mθ and M2 Mθ (59 and 91 for M1 Mθ and M2 Mθ respectively) (**Figure 5 A and 5 B**). When the Oxy-Fe-X zeolite was used and compared to the Fe-X zeolite, a significant change in the expression of 17 proteins was detected for M1 Mθ (9 overexpressed and 8 downregulated) (**Figure 5 C**) while only 6 proteins for M2 Mθ (4 overexpressed and 2 downregulated) (**Figure 5 D**). The outcomes of this study suggest that the addition of nanozeolites has the potential to modulate the expression patterns of various proteins. These results are in line with studies performed at the mRNA level where authors reported that more than 1000 genes were dysregulated after

addition of SPION on M θ [31]. Here, the addition of Fe-X zeolite to M2 M θ resulted in a greater degree of protein dysregulation as compared to M1 M θ , relative to the control condition. In contrast, the addition of Oxy-Fe-X dysregulated a smaller amount of protein on M2 M θ than on M1 M θ . This result is in line with our previous report which demonstrated that M1 M θ exhibits more susceptibility than M2 to alterations in oxygen concentrations [28]. Interestingly, some protein modifications were observed to be related to M θ polarization, as exemplified WDFY1, CD180, and OCAD1 [34,35].

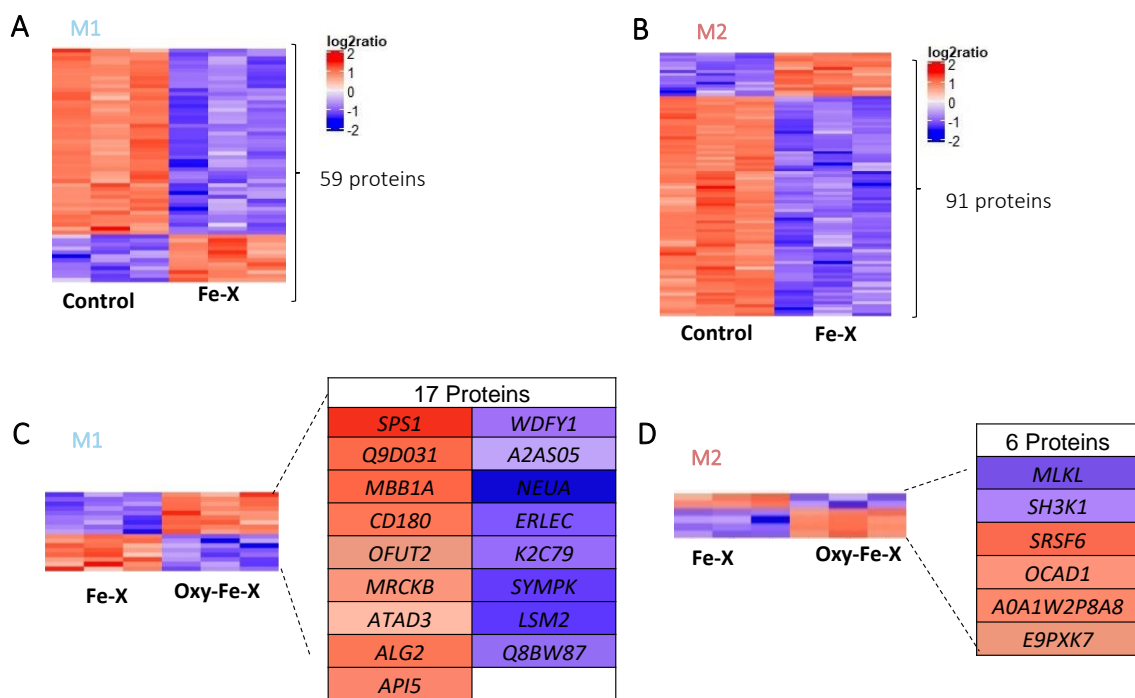


Figure 5: Comparison of protein expression of M1 macrophages exposed to zeolites in hypoxia. A) Visualization of the changes in protein expression between Control M1 macrophages and M1 macrophages exposed to 100 μ g/mL of Fe-X in hypoxia. N=3. **B)** Visualization of the changes in protein expression between Control M2 macrophages and M2 macrophages exposed to 100 μ g/mL of Fe-X in hypoxia. N=3. **C)** Visualization of the changes in protein expression between M1 macrophages exposed to 100 μ g/mL of Fe-X and to 100 μ g/ml of Oxy-Fe-X in hypoxia. N=3. **D)** Visualization of the changes in protein expression between M2 macrophages exposed to 100 μ g/mL of Fe-X and to 100 μ g/ml of Oxy-Fe-X in hypoxia. N=3.

3.4 Impact of zeolites on tumor growth on immunocompetent and immunodeficient models: in vivo study

In order to evaluate the impact of the reoxygenation strategy on M θ polarization in a GBM context, we performed *in vivo* studies. Indeed, M θ are the most abundant inflammatory cells in GBM and reverting their pro-tumoral phenotype could slowdown tumor progression [19]. Two models were used: a human GBM model developed in nude mice and a murine GL261 GBM model developed in C57BL/6 mice. Both models display M θ infiltration and hypoxia [36,37]. Here, the GL261 syngeneic mice model was used to study reoxygenation within an operational immune environment, while the human U251-MG orthotopic xenograft model, albeit lacking T cells in murine models facilitated the examination of relevant aspects in a human context. The tumor progression was followed by MRI imaging with anatomical T2w sequence and the treatment is detailed in **Figure 6 A and D**.

As expected, a noticeable increase in the tumor volume of mice was observed in both models over the course of seven days (**Figure 6 B and E**). For the GL261 model, the tumors at D7 post-treatment show areas of hemorrhages and necrosis. Conversely, the U251-MG was more edematous and more invasive as we already reported. After injection of the zeolite suspension, a tendency toward reduced tumor growth compared to control was noticed for Na-X and Fe-X (**Figure 6 F**) in the U251-MG model. Notably, Oxy-Fe-X failed in showing such an effect in the U251-MG model. However, no detected impact of the nanoparticles was observed for the GL261 model (**Figure 6 C**).

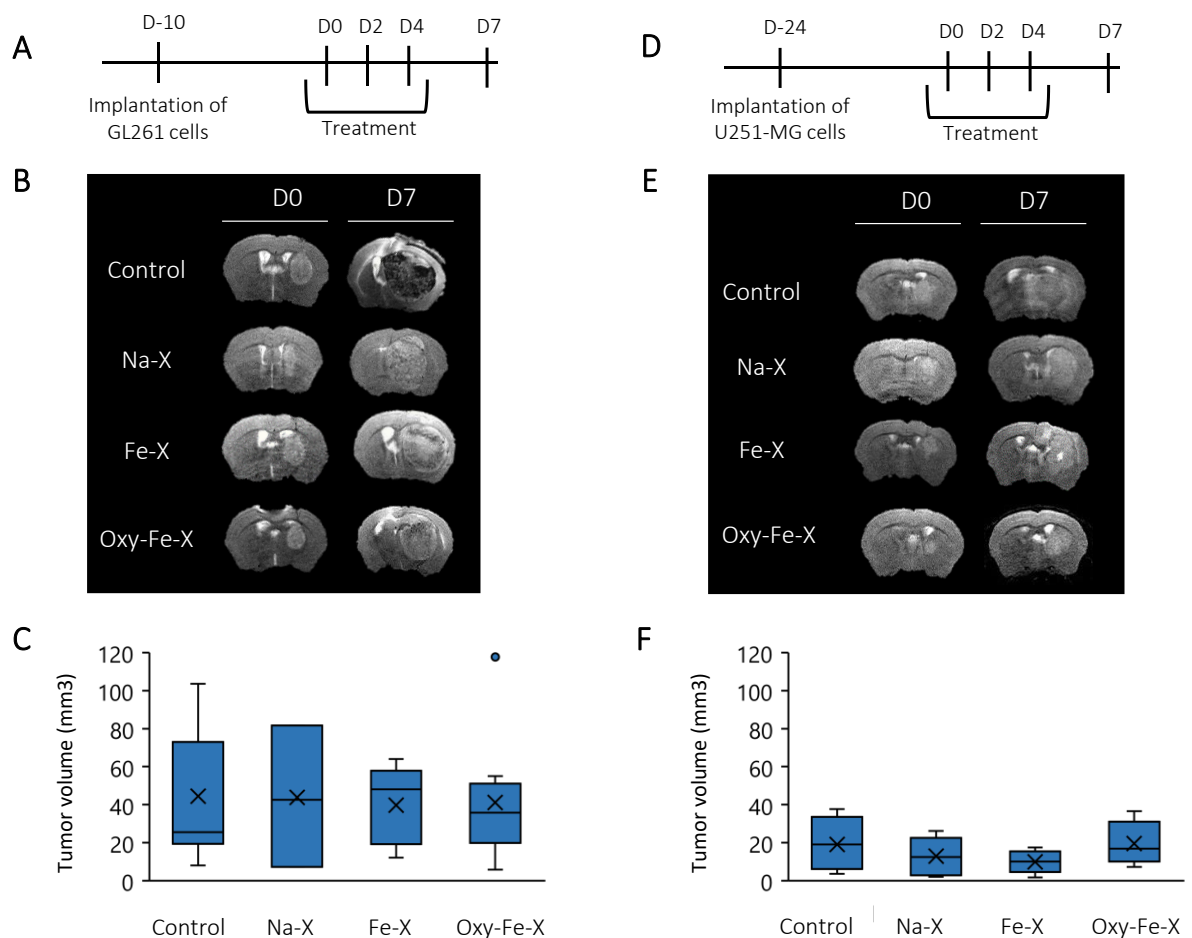


Figure 6: Assessment of the effects of zeolites on tumor growth in an immunocompetent and an immuno-deficient model of GBM. **A)** Experimental protocol for monitoring tumor growth after implantation of GL261 cells. **B)** Visualization of tumors by T2 MRI imaging before treatment (D0) and after treatment (D7) of groups: control; native zeolites (Na-X); zeolites carrying a Fe cation (Fe-X) and zeolites carrying a Fe cation saturated with oxygen (Oxy-Fe-X). **C)** Quantification of the tumor volumes of the control groups (n=13), Na-X (n=3), Fe-X (n=7) and Oxy-Fe-X (n = 11) before (grey) and after treatments (blue). Mean \pm standard deviation. Kruskal-Wallis nonparametric test and non-significant median test. **D)** Experimental protocol for monitoring tumor progression after implantation of U251-MG cells. **E)** Visualization of tumors by T2 MRI imaging before treatment (D0) and after treatment (D7) of the groups: control; native zeolites (Na-X); zeolites carrying an Fe cation (Fe-X) and zeolites carrying an Fe cation saturated with oxygen (Oxy-Fe-X). **F)** Quantification of tumor volumes of the control

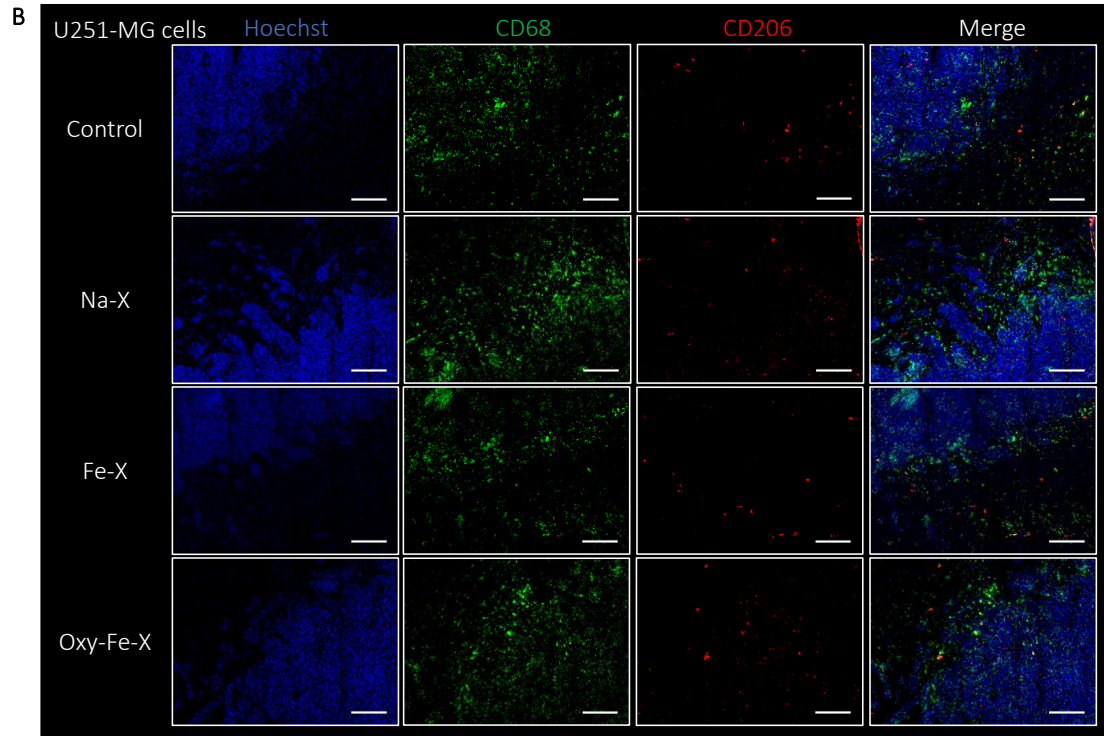
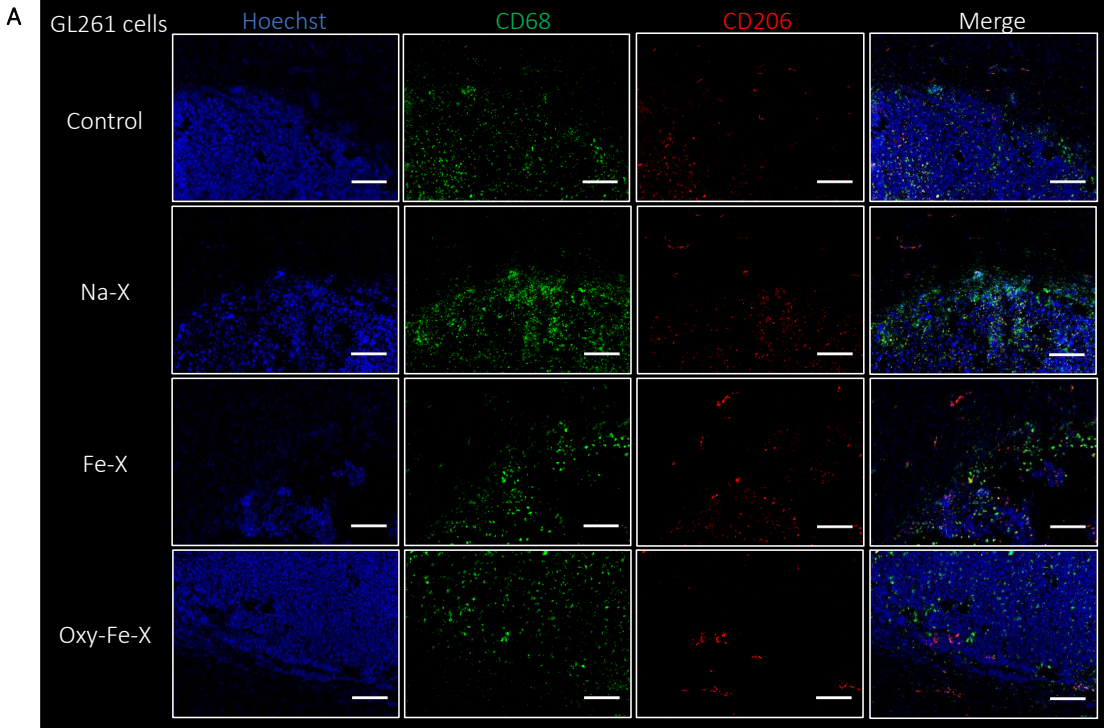
groups (n=8), Na-X (n=6), Fe-X (n=6) and Oxy-Fe-X (n=7) before (grey) and after treatments (blue). Mean \pm standard deviation. Kruskal-wallis nonparametric test and non-significant median test.

3.5 Impact of zeolites on GBM inflammation

The potential effect of zeolites on inflammation of GBM was studied by assessing the presence of M θ and microglia using CD68 immunofluorescence labeling while CD206 staining was rather used to assess M2 like phenotype (**Figure 7 A and B**). Regarding the control group, the CD68 labeling represented on average area coverage $9.28 \pm 8.08\%$ for the GL261 model and $8.24 \pm 2.02\%$ for the U251-MG model (**Figure 7 C and E**), while the CD206 labeling represented on average $2.93 \pm 2.26\%$ and $2.38 \pm 1.93\%$ of the area for the GL261 and U251-MG models, respectively (**Figure 7 D and F**). It should be noticed that M θ (CD68) cells were mainly located on the edge of the tumors while the majority of M2-like M θ infiltrate the tumor core.

The injection of Na-X zeolite suspension in the GL261 immunocompetent model mice did not modify the proportion of M θ or M2-like M θ cells found in tumors (**Figure 7 C**). In contrast, in the U251-MG model, a significant increase in CD68 labeling was noticed in comparison to the control (**Figure 7 D**). Regarding the CD206 labeling, the coverage represented $2.28 \pm 0.29\%$ for the GL261 and $3.05 \pm 1.37\%$ for the U251-MG (**Figure 7 D and F**). However, after injection of Fe-X and Oxy-Fe-X zeolite suspensions, no difference were observed for both models in comparison to the control. The supply of oxygen through the use of Oxy-Fe-X does not present a substantial effect on the infiltration of TAMs.

Leblond *et al.*, showed that the repolarization of macrophages (bone marrow derived macrophages) from M1 to M2 is realizable in an *in vitro* setting, and Laskar *et al.*, showed that the repolarization of M2 to M1 was possible in the presence SPION [23]. In our study, it seems that the involvement of Fe and oxygen is not sufficient for the *in vitro* and *in vivo* repolarization of M2 M θ .



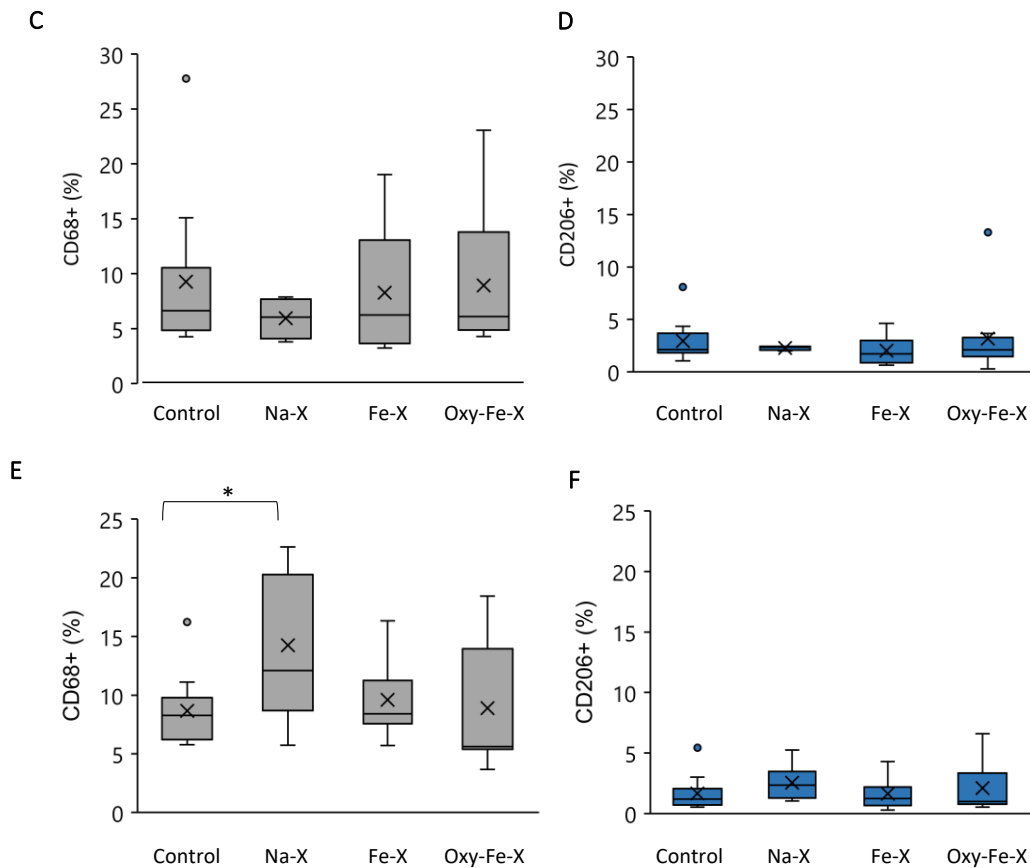


Figure 7: Immunohistological analyzes of the effect of zeolites on tumor inflammation. **A)** Detection of TAMs in a mouse GBM model (GL261). The detection of macrophages and microglia were observed by labeling the CD68 protein (green) and the M2 polarization were observed by labeling the CD206 protein (red) in a GBM model. Scale bar=200 μ m. **B)** Detection of TAMs in a human GBM (U251-MG). Scale bar=200 μ m. **C)** Quantification of CD68 labelling in the GL261 model. **D)** Quantification of CD206 labelling in the GL261 model. **E)** Quantification of CD68 labelling in the U251-MG model. **F)** Quantification of CD206 labeling in the U251-MG model. * $p < 0.05$ after a nonparametric Kruskal-Wallis test ($p = 0.0289$ group effect) and pairwise comparison test; (CD68). ; Non-parametric Kruskal-Wallis test not significant (CD206; $p = 0.45$).

3.6 Impact of O_2 supply by zeolites on tumor hypoxia

The impact of oxygen delivery *via* zeolites on intratumoral hypoxia was studied. We assessed the presence of hypoxia by immunostaining against Carbonic Anhydrase IX (CAIX). For the GL261 model in

control condition, the CAIX labeling revealed the presence of hypoxia around necrotic areas as shown in **Figure 8 A**. The coverage was on average of $3.79 \pm 2.97\%$. The injection of zeolite suspensions Na-X, Fe-X and Oxy-Fe-X was found to have an impact on hypoxia immunostaining in GL261 model, *i.e.* a slight but not significant decrease in the area of CAIX positive immunostaining was observed. For instance, the injection of Oxy-Fe-X resulted in the decrease of the hypoxia areas to $1.73 \pm 1.31\%$ ($p=0.11$ vs control group).

Figure 8 B shows the results from a similar experiment, performed on the immunodeficient model U251-MG. In comparison to the GL261 model, hypoxia is much more obvious in that case. For the control condition, the CAIX labeling covers $9.14 \pm 4.98\%$ of tumor area. It is localized in the center of the tumors with some necrotic areas in individual cases. After the injection of Na-X zeolite suspension, no modification was observed in the CAIX positive area nor in its localization. Similar observations after injections of Fe-X and Oxy-Fe-X zeolite suspensions were detected.

One explanation between these two models could be attributed to the degree of hypoxia. In these experiments, we show that the U251 model is much more hypoxic than the GL261 model. The more pronounced hypoxia observed in the U251 model may explain the greater difficulty to reoxygenate this model. For instance, we showed that the U251 model exhibit reduced sensitivity to hyperoxic/hypercapnic conditions [12] which can be linked to the relatively low vascularity observed within this model.

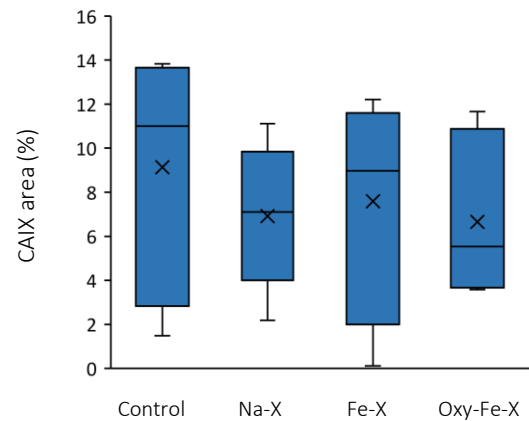
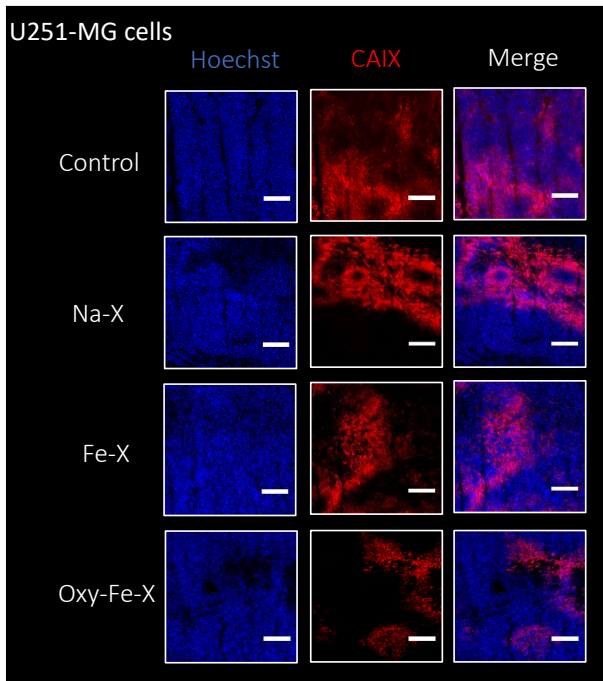
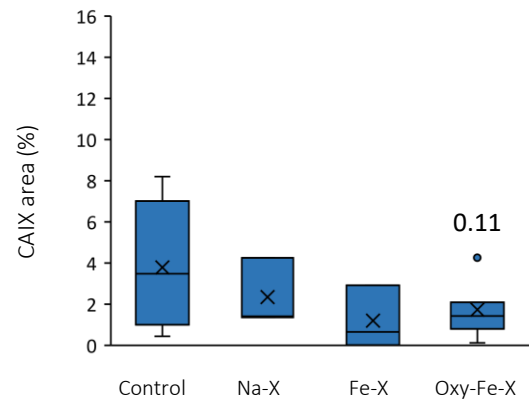
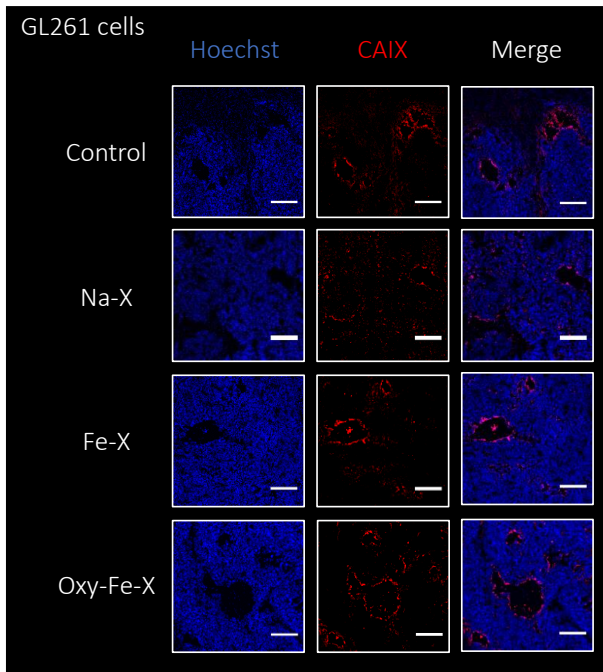


Figure 8: Detection of hypoxia by immunostaining in mouse GBM. A) Visualisation of intratumoral hypoxia of different groups. This detection was observed by labeling the carbonic anhydrase IX protein (Red). The scale bar = 200µm. Quantification of the CAIX protein of GL261 model. **B)** Visualization of intratumoral hypoxia of different groups. This detection was observed by labeling the carbonic anhydrase IX protein (Red). The scale bar = 200µm. Quantification of the CAIX protein of U251-MG model.

4. Conclusions

In summary, the *in vitro* experiments show that zeolites delivered in high concentration seemed to impact the macrophages. Our findings indicate that while cell cycle studies revealed some changes in the cell cycle, no significant effects on cell death were observed. Furthermore, the results of polarization studies demonstrate that the use of zeolites or oxygen delivery *via* zeolites does not alter the macrophage phenotypes. Protein analysis showed that the addition of zeolites to the culture medium resulted in modification to M θ proteins synthesis, particularly for the M2 M θ phenotype under hypoxic condition. However, the oxygen supply *via* Oxy-Fe-X zeolite resulted in more significant changes to proteins expression in the M1 M θ phenotype than in the M2 M θ phenotype. Notably, the proteomic expression profiles of the M1 vs M2, indicated that many proteins are modulated, thus showing a significant difference between these two phenotypes.

When analyzing iNOS and Arginase 1 proteins, we found, despite oxygen saturated Oxy-Fe-X zeolites, that the iNOS expression was still lower for M2 than M1, meanwhile the Arginase 1 still highly expressed by M2 compared to M1 M θ . Based on these proteomic studies, it can be deduced that the supply of oxygen *via* Oxy-Fe-X zeolite does not induce M1 repolarization of M θ *in vitro*. Experiments carried out in mice, including both mouse and human GBM models did not show major effects on tumoral microenvironment. The observation and quantification of M2 M θ revealed a comparable distribution across all injected zeolite suspensions, however, a significantly slight increase in accumulation was observed following Na-X zeolite injection in the U251-MG model. Regarding the hypoxia, no significant modifications were observed. Despite these results, reducing hypoxia still remains a way to restore anti-tumor immunity which also may affect other cells such as lymphocytes [38]. Other polarization strategies involving pharmacological agents that inhibit hypoxia are being investigated [19,39]. As an example, potent pro-M1 strategies have been reported but it is worth

noting that the driving force of hypoxia may still promote M2 macrophages [19]. Our approach could be used in conjunction with these strategies to improve their efficacy.

Credit authorship contribution statement

AF, CH, CJ, RS, BB, LC performed all experiments on cells and animals; SK; SG conducted synthesis and physico-chemical characterizations. SM and SV designed the study and interpreted the data. All authors drafted and edited the MS.

Declaration of competing interest

Nothing to declare.

Funding

The financial support from the Région Normandie, FEDER Program Zeoxy, INCA (INCA11699) and the Centre of zeolites and nanoporous materials, Region Normandie, CNRS (CLEAR) is acknowledged.

Data Availability

Data will be made available on request

References

- [1] P.Y. Wen, M. Weller, E.Q. Lee, B.A. Alexander, J.S. Barnholtz-Sloan, F.P. Barthel, T.T. Batchelor, R.S. Bindra, S.M. Chang, E.A. Chiocca, T.F. Cloughesy, J.F. DeGroot, E. Galanis, M.R. Gilbert, M.E. Hegi, C. Horbinski, R.Y. Huang, A.B. Lassman, E. Le Rhun, M. Lim, M.P. Mehta, I.K. Mellingshoff, G. Minniti, D. Nathanson, M. Platten, M. Preusser, P. Roth, M. Sanson, D. Schiff, S.C. Short, M.J.B. Taphoorn, J.-C. Tonn, J. Tsang, R.G.W. Verhaak, A. von Deimling, W. Wick, G. Zadeh, D.A. Reardon, K.D. Aldape, M.J. van den Bent, Glioblastoma in Adults: A Society for Neuro-Oncology (SNO) and European Society of Neuro-Oncology (EANO) Consensus Review on Current Management and Future Directions, *Neuro-Oncol.* (2020).
<https://doi.org/10.1093/neuonc/noaa106>.
- [2] C. Roma-Rodrigues, R. Mendes, P.V. Baptista, A.R. Fernandes, Targeting Tumor Microenvironment for Cancer Therapy, *Int. J. Mol. Sci.* 20 (2019) E840.
<https://doi.org/10.3390/ijms20040840>.
- [3] L. Bekaert, S. Valable, E. Lechapt-Zalcman, K. Ponte, S. Collet, J.-M. Constans, G. Levallet, K. Bordji, E. Petit, P. Branger, E. Emery, A. Manrique, L. Barré, M. Bernaudin, J.-S. Guillamo, [18F]-FMISO PET study of hypoxia in gliomas before surgery: correlation with molecular markers of hypoxia and angiogenesis, *Eur. J. Nucl. Med. Mol. Imaging.* 44 (2017) 1383–1392.
<https://doi.org/10.1007/s00259-017-3677-5>.
- [4] A. Chakhoyan, J.-S. Guillamo, S. Collet, F. Kauffmann, N. Delcroix, E. Lechapt-Zalcman, J.-M. Constans, E. Petit, E.T. MacKenzie, L. Barré, M. Bernaudin, O. Touzani, S. Valable, FMISO-PET-

- derived brain oxygen tension maps: application to glioblastoma and less aggressive gliomas, *Sci. Rep.* 7 (2017) 10210. <https://doi.org/10.1038/s41598-017-08646-y>.
- [5] D.R. Collingridge, J.M. Piepmeier, S. Rockwell, J.P. Knisely, Polarographic measurements of oxygen tension in human glioma and surrounding peritumoural brain tissue, *Radiother. Oncol. J. Eur. Soc. Ther. Radiol. Oncol.* 53 (1999) 127–131.
- [6] R. Rampling, G. Cruickshank, A.D. Lewis, S.A. Fitzsimmons, P. Workman, Direct measurement of pO₂ distribution and bioreductive enzymes in human malignant brain tumors, *Int. J. Radiat. Oncol. Biol. Phys.* 29 (1994) 427–431.
- [7] H. Kempf, M. Bleicher, M. Meyer-Hermann, Spatio-Temporal Dynamics of Hypoxia during Radiotherapy, *PLoS One.* 10 (2015) e0133357. <https://doi.org/10.1371/journal.pone.0133357>.
- [8] B.F. Jordan, P. Sonveaux, Targeting tumor perfusion and oxygenation to improve the outcome of anticancer therapy, *Front. Pharmacol.* 3 (2012) 94. <https://doi.org/10.3389/fphar.2012.00094>.
- [9] A.R. Monteiro, R. Hill, G.J. Pilkington, P.A. Madureira, The Role of Hypoxia in Glioblastoma Invasion, *Cells.* 6 (2017) E45. <https://doi.org/10.3390/cells6040045>.
- [10] A.L. Chédeville, P.A. Madureira, The Role of Hypoxia in Glioblastoma Radiotherapy Resistance, *Cancers.* 13 (2021) 542. <https://doi.org/10.3390/cancers13030542>.
- [11] S. Valable, A.N. Gérault, G. Lambert, M.M. Leblond, C. Anfray, J. Toutain, K. Bordji, E. Petit, M. Bernaudin, E.A. Pérès, Impact of Hypoxia on Carbon Ion Therapy in Glioblastoma Cells: Modulation by LET and Hypoxia-Dependent Genes, *Cancers.* 12 (2020). <https://doi.org/10.3390/cancers12082019>.
- [12] A. Chakhoyan, A. Corroyer-Dulmont, M.M. Leblond, A. Gérault, J. Toutain, L. Chazaviel, D. Divoux, E. Petit, E.T. MacKenzie, F. Kauffmann, N. Delcroix, M. Bernaudin, O. Touzani, S. Valable, Carbogen-induced increases in tumor oxygenation depend on the vascular status of the tumor: A multiparametric MRI study in two rat glioblastoma models, *J. Cereb. Blood Flow Metab. Off. J. Int. Soc. Cereb. Blood Flow Metab.* 37 (2016) 2270–2282. <https://doi.org/10.1177/0271678X16663947>.
- [13] R. Miralbell, F. Mornex, R. Greiner, M. Bolla, G. Storme, M. Hulshof, J. Bernier, J. Denekamp, A.M. Rojas, M. Pierart, M. van Glabbeke, R.O. Mirimanoff, Accelerated radiotherapy, carbogen, and nicotinamide in glioblastoma multiforme: report of European Organization for Research and Treatment of Cancer trial 22933, *J. Clin. Oncol. Off. J. Am. Soc. Clin. Oncol.* 17 (1999) 3143–3149.
- [14] H. Hou, V. Krishnamurthy Nemani, G. Du, R. Montano, R. Song, B. Gimi, H.M. Swartz, A. Eastman, N. Khan, Monitoring oxygen levels in orthotopic human glioma xenograft following carbogen inhalation and chemotherapy by implantable resonator-based oximetry, *Int. J. Cancer J. Int. Cancer.* 136 (2015) 1688–1696. <https://doi.org/10.1002/ijc.29132>.
- [15] C. Anfray, S. Komaty, A. Corroyer-Dulmont, M. Zaarour, C. Helaine, H. Ozcelik, C. Allieux, J. Toutain, K. Goldyn, E. Petit, K. Bordji, M. Bernaudin, V. Valtchev, O. Touzani, S. Mintova, S. Valable, Nanosized zeolites as a gas delivery platform in a glioblastoma model, *Biomaterials.* 257 (2020) 120249. <https://doi.org/10.1016/j.biomaterials.2020.120249>.
- [16] Y.T. Yeung, K.L. McDonald, T. Grewal, L. Munoz, Interleukins in glioblastoma pathophysiology: implications for therapy, *Br. J. Pharmacol.* 168 (2013) 591–606. <https://doi.org/10.1111/bph.12008>.
- [17] F. Klemm, R.R. Maas, R.L. Bowman, M. Kornete, K. Soukup, S. Nassiri, J.-P. Brouland, C.A. Iacobuzio-Donahue, C. Brennan, V. Tabar, P.H. Gutin, R.T. Daniel, M.E. Hegi, J.A. Joyce, Interrogation of the Microenvironmental Landscape in Brain Tumors Reveals Disease-Specific Alterations of Immune Cells, *Cell.* 181 (2020) 1643–1660.e17. <https://doi.org/10.1016/j.cell.2020.05.007>.
- [18] A. Mantovani, P. Allavena, F. Marchesi, C. Garlanda, Macrophages as tools and targets in cancer therapy, *Nat. Rev. Drug Discov.* 21 (2022) 799–820. <https://doi.org/10.1038/s41573-022-00520-5>.

- [19] S.M. Pyonteck, L. Akkari, A.J. Schuhmacher, R.L. Bowman, L. Sevenich, D.F. Quail, O.C. Olson, M.L. Quick, J.T. Huse, V. Teijeiro, M. Setty, C.S. Leslie, Y. Oei, A. Pedraza, J. Zhang, C.W. Brennan, J.C. Sutton, E.C. Holland, D. Daniel, J.A. Joyce, CSF-1R inhibition alters macrophage polarization and blocks glioma progression, *Nat. Med.* 19 (2013) 1264–1272. <https://doi.org/10.1038/nm.3337>.
- [20] C. Lan, X. Huang, S. Lin, H. Huang, Q. Cai, T. Wan, J. Lu, J. Liu, Expression of M2-Polarized Macrophages is Associated with Poor Prognosis for Advanced Epithelial Ovarian Cancer, *Technol. Cancer Res. Treat.* 12 (2013) 259–267. <https://doi.org/10.7785/tcrt.2012.500312>.
- [21] M.M. Leblond, A.N. G erault, A. Corroyer-Dulmont, E.T. MacKenzie, E. Petit, M. Bernaudin, S. Valable, Hypoxia induces macrophage polarization and re-education toward an M2 phenotype in U87 and U251 glioblastoma models, *Oncoimmunology*. 5 (2016) e1056442. <https://doi.org/10.1080/2162402X.2015.1056442>.
- [22] L. Akkari, R.L. Bowman, J. Tessier, F. Klemm, S.M. Handgraaf, M. de Groot, D.F. Quail, L. Tillard, J. Gadiot, J.T. Huse, D. Brandsma, J. Westerga, C. Watts, J.A. Joyce, Dynamic changes in glioma macrophage populations after radiotherapy reveal CSF-1R inhibition as a strategy to overcome resistance, *Sci. Transl. Med.* 12 (2020). <https://doi.org/10.1126/scitranslmed.aaw7843>.
- [23] A. Laskar, J. Eilertsen, W. Li, X.-M. Yuan, SPION primes THP1 derived M2 macrophages towards M1-like macrophages, *Biochem. Biophys. Res. Commun.* 441 (2013) 737–742. <https://doi.org/10.1016/j.bbrc.2013.10.115>.
- [24] M. Costa da Silva, M.O. Breckwoltd, F. Vinchi, M.P. Correia, A. Stojanovic, C.M. Thielmann, M. Meister, T. Muley, A. Warth, M. Platten, M.W. Hentze, A. Cerwenka, M.U. Muckenthaler, Iron Induces Anti-tumor Activity in Tumor-Associated Macrophages, *Front. Immunol.* 8 (2017) 1479. <https://doi.org/10.3389/fimmu.2017.01479>.
- [25] S. Komaty, A. Daouli, M. Badawi, C. Anfray, M. Zaarour, V. Samuel, S. Mintova, Incorporation of trivalent cations in NaX zeolite nanocrystals for the adsorption of O₂ in the presence of CO₂, *Phys. Chem. Chem. Phys.* 22 (2020) 9934–9942. <https://doi.org/10.1039/D0CP00111B>.
- [26] R. Fischer, B.M. Kessler, Gel-aided sample preparation (GASP)--a simplified method for gel-assisted proteomic sample generation from protein extracts and intact cells, *Proteomics*. 15 (2015) 1224–1229. <https://doi.org/10.1002/pmic.201400436>.
- [27] C.A. Schneider, W.S. Rasband, K.W. Eliceiri, NIH Image to ImageJ: 25 years of image analysis, *Nat. Methods*. 9 (2012) 671–675. <https://doi.org/10.1038/nmeth.2089>.
- [28] M.M. Leblond, A.N. G erault, A. Corroyer-Dulmont, E.T. MacKenzie, E. Petit, M. Bernaudin, S. Valable, Hypoxia induces macrophage polarization and re-education toward an M2 phenotype in U87 and U251 glioblastoma models, *Oncoimmunology*. 5 (2016) e1056442. <https://doi.org/10.1080/2162402X.2015.1056442>.
- [29] M.M. Leblond, E.A. P er es, C. Helaine, A.N. G erault, D. Moulin, C. Anfray, D. Divoux, E. Petit, M.B.S. Valable, M.M. Leblond, E.A. P er es, C. Helaine, A.N. G erault, D. Moulin, C. Anfray, D. Divoux, E. Petit, M. Bernaudin Samuel Valable, M2 macrophages are more resistant than M1 macrophages following radiation therapy in the context of glioblastoma, *Oncotarget*. 8 (2017) 72597–72612. <https://doi.org/10.18632/oncotarget.19994>.
- [30] D. Reichel, M. Tripathi, J.M. Perez, Biological Effects of Nanoparticles on Macrophage Polarization in the Tumor Microenvironment, *Nanotheranostics*. 3 (2019) 66–88. <https://doi.org/10.7150/ntno.30052>.
- [31] V. Kodali, M.H. Littke, S.C. Tilton, J.G. Teegarden, L. Shi, C.W. Frevert, W. Wang, J.G. Pounds, B.D. Thrall, Dysregulation of macrophage activation profiles by engineered nanoparticles, *ACS Nano*. 7 (2013) 6997–7010. <https://doi.org/10.1021/nn402145t>.
- [32] S. Komaty, H.  z celik, M. Zaarour, A. Ferre, S. Valable, S. Mintova, Ruthenium tris(2,2'-bipyridyl) complex encapsulated in nanosized faujasite zeolite as intracellular localization tracer, *J. Colloid Interface Sci.* 581 (2021) 919–927. <https://doi.org/10.1016/j.jcis.2020.08.117>.
- [33] J.M. Rojas, L. Sanz-Ortega, V. Mulens-Arias, L. Guti errez, S. P erez-Yag ue, D.F. Barber, Superparamagnetic iron oxide nanoparticle uptake alters M2 macrophage phenotype, iron

- metabolism, migration and invasion, *Nanomedicine Nanotechnol. Biol. Med.* 12 (2016) 1127–1138. <https://doi.org/10.1016/j.nano.2015.11.020>.
- [34] S. Rahman, J. Vandewalle, P.H.P. van Hamersveld, C. Verseijden, O. Welting, A. Jongejan, P. Casanova, S.L. Meijer, C. Libert, T.B.M. Hakvoort, W.J. de Jonge, S.E.M. Heinsbroek, miR-511 Deficiency Protects Mice from Experimental Colitis by Reducing TLR3 and TLR4 Responses via WD Repeat and FYVE-Domain-Containing Protein 1, *Cells*. 11 (2021) 58. <https://doi.org/10.3390/cells11010058>.
- [35] Y. Yang, C. Wang, P. Cheng, X. Zhang, X. Li, Y. Hu, F. Xu, F. Hong, G. Dong, H. Xiong, CD180 Ligation Inhibits TLR7- and TLR9-Mediated Activation of Macrophages and Dendritic Cells Through the Lyn-SHP-1/2 Axis in Murine Lupus, *Front. Immunol.* 9 (2018) 2643. <https://doi.org/10.3389/fimmu.2018.02643>.
- [36] C. Helaine, A.E. Ferré, M.M. Leblond, E.A. Pérès, M. Bernaudin, S. Valable, E. Petit, Angiopoietin-2 Combined with Radiochemotherapy Impedes Glioblastoma Recurrence by Acting in an Autocrine and Paracrine Manner: A Preclinical Study, *Cancers*. 12 (2020) E3585. <https://doi.org/10.3390/cancers12123585>.
- [37] A. Corroyer-Dulmont, E.A. Pérès, E. Petit, L. Durand, L. Marteau, J. Toutain, D. Divoux, S. Roussel, E.T. MacKenzie, L. Barré, M. Bernaudin, S. Valable, Noninvasive assessment of hypoxia with 3-[¹⁸F]-fluoro-1-(2-nitro-1-imidazolyl)-2-propanol ([¹⁸F]-FMISO): a PET study in two experimental models of human glioma, *Biol. Chem.* 394 (2013) 529–539. <https://doi.org/10.1515/hsz-2012-0318>.
- [38] J.H. Park, H.-J. Kim, C.W. Kim, H.C. Kim, Y. Jung, H.-S. Lee, Y. Lee, Y.S. Ju, J.E. Oh, S.-H. Park, J.H. Lee, S.K. Lee, H.K. Lee, Tumor hypoxia represses $\gamma\delta$ T cell-mediated antitumor immunity against brain tumors, *Nat. Immunol.* 22 (2021) 336–346. <https://doi.org/10.1038/s41590-020-00860-7>.
- [39] D. Yan, J. Kowal, L. Akkari, A.J. Schuhmacher, J.T. Huse, B.L. West, J.A. Joyce, Inhibition of colony stimulating factor-1 receptor abrogates microenvironment-mediated therapeutic resistance in gliomas, *Oncogene*. 36 (2017) 6049–6058. <https://doi.org/10.1038/onc.2017.261>.